Materials Research Express

Effect of carrier doping on the electronic states of earth-abundant Fe–Al–Si thermoelectric materials

Materials Research Express

PAPER

Effect of carrier doping on the electronic states of earth-abundant Fe–Al–Si thermoelectric materials

Shunsuke Tsuda[1], **Asako Yoshinari**[1,2], **Shingo Takezawa**[1,2], **Kenta Ohishi**[1,2], **Naoka Nagamura**[1,2,3], **Wenxiong Zhang**[4], **Yutaka Iwasaki**[5] and **Yoshiki Takagiwa**[5]

[1] Photoemission Group, National Institute for Materials Science, 3-13 Sakura, Tsukuba, Ibaraki 305-0003, Japan
[2] Graduate School of Advanced Engineering, Tokyo University of Science, 6-3-1 Niijuku, Katsushika, Tokyo 125-8585, Japan
[3] PRESTO, Japan Science and Technology Agency, 4-1-8, Honcho, Kawaguchi-shi, Saitama 332-0012, Japan
[4] Institute for Solid State Physics, The University of Tokyo, 5-1-5 Kashiwa, Chiba 277-8581, Japan
[5] Thermoelectric Materials Group, National Institute for Materials Science, 1-2-1 Sengen, Tsukuba, Ibaraki 305-0047, Japan

E-mail: TSUDA.Shunsuke@nims.go.jp

Keywords: thermoelectric materials, electronic state, photoemission spectroscopy, pn control, $Fe_3Al_2Si_3$

OPEN ACCESS

RECEIVED
13 February 2023

REVISED
25 April 2023

ACCEPTED FOR PUBLICATION
10 May 2023

PUBLISHED
26 May 2023

Abstract

Fe–Al–Si-based thermoelectric (FAST) materials are non-toxic and low-cost materials that can be used for autonomous power supplies to drive internet-of-things wireless sensor devices. The conduction type can be controlled by changing the Al/Si ratio, which is suitable for fabricating reliable thermoelectric power-generation modules consisting of materials with similar thermal expansion coefficients. In this work, we evaluated the electronic structures of p- and n-type FAST materials with relatively large absolute values of the Seebeck coefficient by photoemission spectroscopy to obtain deeper insight into controlling the p-n characteristics of FAST materials. The core-level spectra suggested that the FAST materials have a covalent bonding nature. The chemical-potential shift should be the dominant factor of the core-level shift, which is consistent with the expected behavior of carrier doping of thermoelectric semiconductors, that is, rigid-band-like behavior. The size of the core-level shift of ~0.15 eV is close to the band gap of ~0.18 eV obtained from transport measurements. The observed electronic structure can qualitatively explain the experimental results.

1. Introduction

Thermoelectric materials are attractive for use in driving internet-of-things wireless sensor devices, which require a power output of at least a few hundred microwatts using low-temperature waste heat sources at temperatures less than 500 K. Thermoelectric materials are evaluated by the figure of merit z, which corresponds to the energy-conversion efficiency:

$$z = \frac{S^2\sigma}{\kappa}, \tag{1}$$

where S, σ, and κ are the Seebeck coefficient, electrical conductivity, and thermal conductivity, respectively [1]. To obtain higher power output, materials with a large power factor $S^2\sigma$ and a low κ value to maintain a temperature difference need to be developed. Many novel thermoelectric materials with high z values and power-generation modules using these thermoelectric materials have been investigated [2] based on new concepts and guiding principles [3].

When considering practical use of thermoelectric power-generation devices, the thermoelectric materials should consist of readily available elements, that is, low-cost materials such as β-$FeSi_2$ [4], $MnSi_\gamma$ [5], Fe_2VAl Heusler compounds [6], Mg-Ag-Sb/Mg-Bi-Sb-Te [7], Cu-S [8], and Zn-Sb [9]. Recently reported Earth-abundant Fe–Al–Si (τ_1-$Fe_3Al_2Si_3$) ternary thermoelectric materials [10, 11], which are called FAST materials [12, 13], are promising candidates for fabricating robust power-generation modules using low-temperature waste heat at temperatures less than 500 K [13] because they have excellent oxidation resistance and mechanical properties [14]. Takagiwa *et al* have demonstrated operation of temperature/humidity sensors and wireless

transmission by Bluetooth low-energy communication with power-generation modules using p- and n-type FAST materials [12].

From a physical point of view, the τ_1-$Fe_3Al_2Si_3$ compound is a narrow-band-gap semiconductor, as expected from first-principles calculations [10, 15]. The conduction type can be controlled by tuning the Al/Si ratio with a constant Fe concentration without chemical doping/substitution [10, 16], which is suitable for fabricating reliable thermoelectric power-generation modules consisting of materials with similar thermal expansion coefficients [12]. Another way to control the p-n characteristics is chemical doping through elemental substitution. Shiota *et al* [17] synthesized p- and n-type materials by Mn and Co substitution, and the obtained S values at 300 K were 100 and -125 μV K^{-1}, respectively. Recently, the effect of ε-FeSi precipitation on the thermoelectric properties has been discussed by Srinithi *et al* [18]. The single-phase p-FAST sample showed a high S value of ~140 μV K^{-1} at 300 K, but a lower σ value of ~90 Ω^{-1} cm^{-1} at the same temperature. In contrast, the sample with the ε-FeSi phase (5−10% areal fraction) showed a slightly lower S value of ~100 μV K^{-1} at 300 K, but it had a 7-times higher σ value of ~670 Ω^{-1} cm^{-1}. In this case, the sample containing the metallic secondary phase ε-FeSi had a much higher $S^2\sigma$ value of ~880 μW m^{-1} K^{-2} for the p-FAST material. However, there is no report on the same effect for the n-FAST material. These results indicate that both precise carrier concentration tuning with or without chemical doping and microstructure engineering are beneficial to improve the thermoelectric performance of FAST materials.

The band gap and band gap formation mechanism of unconventional intermetallic compounds have been extensively investigated [19, 20]. It is naturally expected the materials composed of metallic constituents have metallic character, but hybridization between transition metals and group III (Al, Ga, In) and IV (Si) elements leads to hollows and pseudogaps in the electronic density of states [20]. Formation of a narrow band gap of a few hundred millielectronvolts near the Fermi level is expected to result in a large absolute value of S even at 300 K. Fredrickson *et al* [21, 22] pointed out that late-transition-metal Nowotny chimney ladder phases, such as binary $RuAl_2$ and $RuGa_2$ compounds, follow the 14-electron rule. This electron-counting rule is a crucial factor for stabilizing intermetallic phases exhibiting structural diversity [23]. Regarding the τ_1-$Fe_3Al_2Si_3$ compound, Hou *et al* [15] reported that the valence bands are mainly because of hybridization of the Fe 3d state with the Si and Al 3p states, and the conduction-band edge is mainly composed of the Fe 3d state and Si 3p state. Therefore, the Fe 3d state is the dominant contribution at the top of the valence bands and bottom of the conduction bands of the τ_1-$Fe_3Al_2Si_3$ compound [15]. Therefore, clarifying the underlying mechanism of band gap formation is crucial to design functional materials, including thermoelectric semiconductors [24].

To better understand the intrinsic thermoelectric characteristics of FAST materials, the electronic structure, including the magnitude of the band gap [25] and formation of impurity states [26], needs to be experimentally investigated. High-quality single crystals with sufficiently large sizes are required to investigate such physical properties. However, growth of single crystals of FAST materials is challenging because the τ_1-$Fe_3Al_2Si_3$ phase forms through a peritectic reaction of liquid and ε-FeSi phases, which is the main reason for the remaining of ε-FeSi phase even after annealing. Thus, it is necessary to fabricate the single-phase samples of the τ_1-$Fe_3Al_2Si_3$ phase with precise composition control [27, 28]. In this work, we investigated the electronic structures of polycrystalline p- and n-type FAST materials by photoemission spectroscopy to obtain deeper insight into controlling the p-n characteristics to enhance the thermoelectric properties of FAST materials.

2. Experimental procedure

The high-purity starting materials Fe (99.9%), Al (99.99%), and Si (99.999%) with nominal compositions of $Fe_{38}Al_{22}Si_{40-x}$ ($x = 0$ and 2.2 for the n- and p-type FAST materials, respectively) were melted using an induction-heating apparatus (NEV-M series; Nisshin Giken Co., Saitama, Japan). High-purity and dense bulk samples without cracks and pores were then synthesized as follows. First, the mother ingots were crushed to fine particles using a mixer-milling apparatus (MI250; IKA Japan, Osaka, Japan). The milled powder samples were then placed in a graphite die with an inner diameter of 10 mm for spark plasma sintering (LABOX-110MC; SinterLand, Inc., Niigata, Japan). The sintering temperatures were 1203–1213 K, and the applied pressure was set to 57 MPa in a purified argon atmosphere. Finally, the sintered bulk samples were annealed at 1173 K for 24 h in a purified argon atmosphere (MILA-5000; Advance Riko, Inc., Kanagawa, Japan) to improve the purity of the τ_1-$Fe_3Al_2Si_3$ phase.

The synthesized bulk samples were characterized by x-ray diffraction (XRD) using Cr $K\alpha$ radiation (Mini-Flex 600; Rigaku, Inc., Tokyo, Japan). The mapping measurements of S were performed at room temperature with 20 μm intervals using a scanning thermal probe micro-imaging apparatus (STPM-1000; Advance Riko, Inc., Kanagawa, Japan). The σ and S values of the samples were measured in the temperature range from 300 to 873 K by four-probe and steady-state temperature gradient methods, respectively (ZEM-3; Advance Riko, Inc., Kanagawa, Japan). We set values of $\Delta T = 10$, 15, and 20 K between the top and bottom of the measured samples.

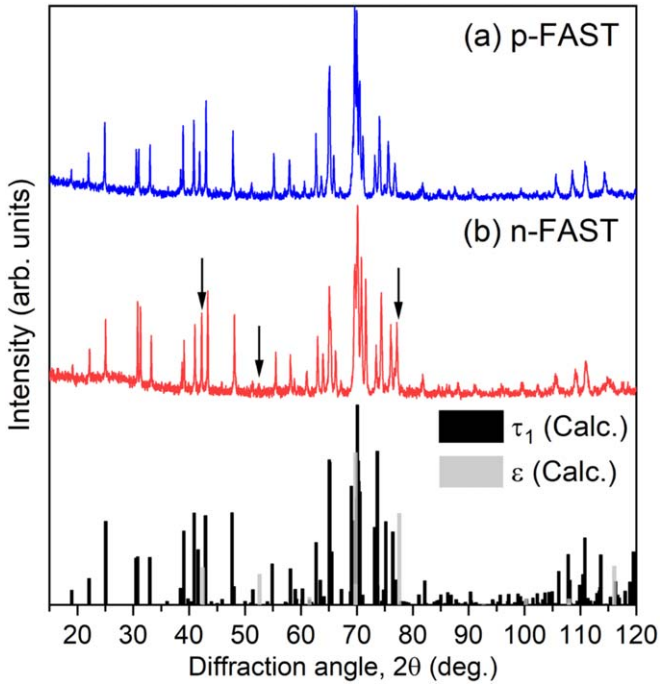

Figure 1. X-ray diffraction patterns of the (a) p-FAST and (b) n-FAST materials, together with the calculated patterns of the τ_1-$Fe_3Al_2Si_3$ and ε-FeSi phases. Arrows indicate peaks from ε-FeSi phase.

The actual ΔT value between the electrodes used to measure the voltage was less than 3 K during the measurements to obtain accurate S values.

The photoemission measurements were performed at beamline BL07LSU of SPring-8 [29]. The excitation energy was set to ~1000 eV. All of the measurements were performed at room temperature. The incident light was focused down to ~200 nm using a Fresnel zone plate. The beam direction was normal to the sample surface. The incident light polarization was horizontal. The photoemission spectra were recorded by a VG Scienta (Scienta Omicron) R3000 electron analyzer with an EWAL lens, which allowed us to correct the photoelectron of an extremely wide angle of $\pm 30^\circ$. The polarization direction and slit of the electron analyzer were in the same plane. The clean sample surface was obtained by in situ fracturing. The binding-energy calibration was performed by a Fermi edge and the $4f_{7/2}$ core level of gold evaporated close to the samples. The energy resolution was ~200 meV. All of the reported spectra are the spectra after subtraction of the Shirley-type background [30], except for the valence-band spectra.

3. Results and discussion

3.1. Phase characterization and thermoelectric properties

The XRD patterns of the synthesized p- and n-type FAST materials, abbreviated as the p-FAST and n-FAST materials, are shown in figure 1. The obtained patterns were identified with the τ_1-$Fe_3Al_2Si_3$ phase. However, we found that both samples contained a small amount of the secondary phase ε-FeSi. From the reference intensity ratio method using Rigaku-PDXL software, the estimated amounts of ε-FeSi were less than 1 and 4 wt.% for the p- and n-FAST materials, respectively.

The mapping results of S at room temperature for the p- and n-FAST materials are shown in figure 2. The averaged $|S|$ values were ~130 and ~110 μV K^{-1} for the p- and n-FAST materials, which quantitatively agreed with the S results at 300 K (figure 3(b)). In both the p- and n-FAST materials, ~20 μm precipitates (black or deep-blue dots) of an Al-doped ε-FeSi phase with a low S value can be clearly observed in figure 2. The amounts of the precipitates were comparable with those obtained from XRD measurements. We note here that the synthesized FAST materials have composite microstructures with ε-phase, which brings a composition deviation of τ_1-phase area from the nominal compositions.

The thermoelectric properties of the p- and n-FAST materials as a function of the temperature are shown in figure 3. The observed thermoelectric properties were typical of semiconducting transport behavior. The room temperature σ values of the p- and n-FAST materials were 300 and 470 Ω^{-1} cm^{-1}, and the S values at 300 K were relatively high values of 140 and -120 μV K^{-1}, respectively. Although the results of the n-FAST material agreed

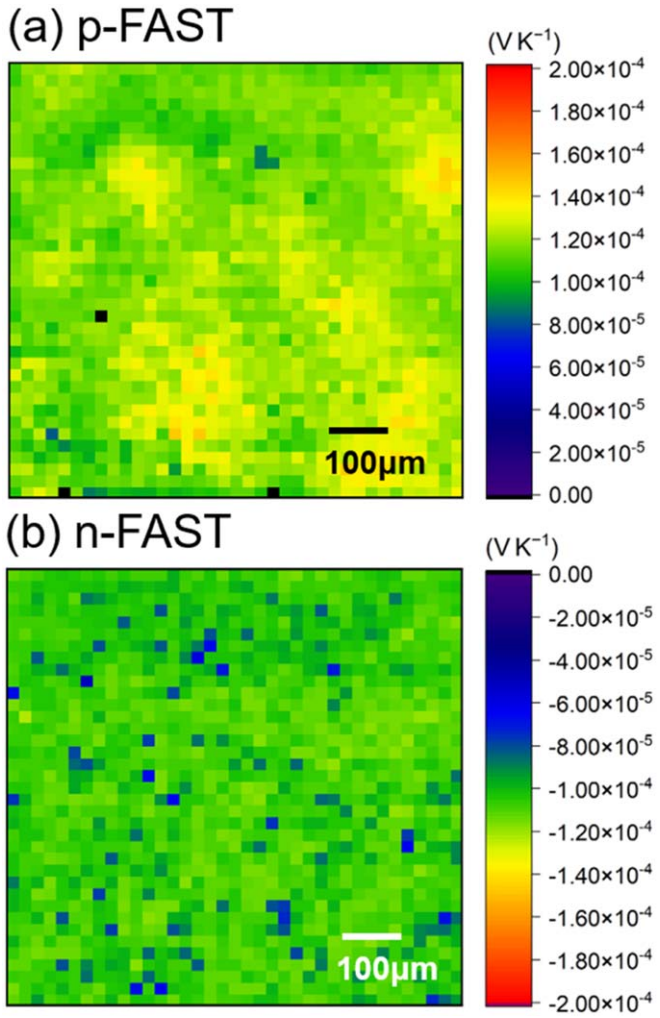

Figure 2. Mapping results of the Seebeck coefficient at room temperature for the (a) p-FAST and (b) n-FAST materials.

with those of a previous sample synthesized by induction-heating and gas-atomization processes [12], the p-FAST material had a lower σ value but a higher S value. This is attributed to the lower carrier concentration in the p-FAST material. As a result, the obtained $S^2\sigma$ value of ~880 μW m^{-1} K^{-2} for the n-type FAST material was similar to that of the highest $S^2\sigma$ sample of p-FAST materials [18]. In contrast, compared with the sample synthesized by induction-heating and gas-atomization processes [12], the p-FAST sample exhibited a slightly lower $S^2\sigma$ value of ~680 μW m^{-1} K^{-2}. The observed sharp decrease in $S^2\sigma$ at temperatures above ~500 K for the p- and n-FAST materials is attributed to a significant reduction of S because of the excitation of minority carriers. Such minority carrier excitation easily occurs in narrow-band gap (typically <0.3 eV) compounds. Indeed, the calculated band gaps from the Arrhenius plot were ~0.18 eV for the p- and n-FAST materials, as shown in figure 4.

From first-principles calculations of the stoichiometric τ_1-$Fe_3Al_2Si_3$ phase [10, 15], the effective mass (m^*) of the conduction band is larger than that of the valence bands, indicating that the carrier mobility of the p-FAST material is higher than that of the n-FAST material. In contrast, the carrier concentration of the n-FAST material should be higher than that of the p-FAST material because of the large electronic density of states at the Fermi level. As a result, the same order of σ was observed for the p- and n-FAST materials, as shown in figure 2(a). However, the validity of rigid band approximation by changing the Al/Si ratio remains to be experimentally verified.

3.2. Photoemission spectra

A typical survey scan spectrum of the n-FAST material is shown in figure 5. All of the peaks can be assigned, as indicated in the figure. Although the measured samples were fractured in the vacuum chamber, the observed O 1s, O auger (KLL), and C 1s peaks could originate from the oxidized starting materials (Fe, Al, and Si) and/or adsorbed residual gas molecules in the ultrahigh vacuum chamber, such as CO_2.

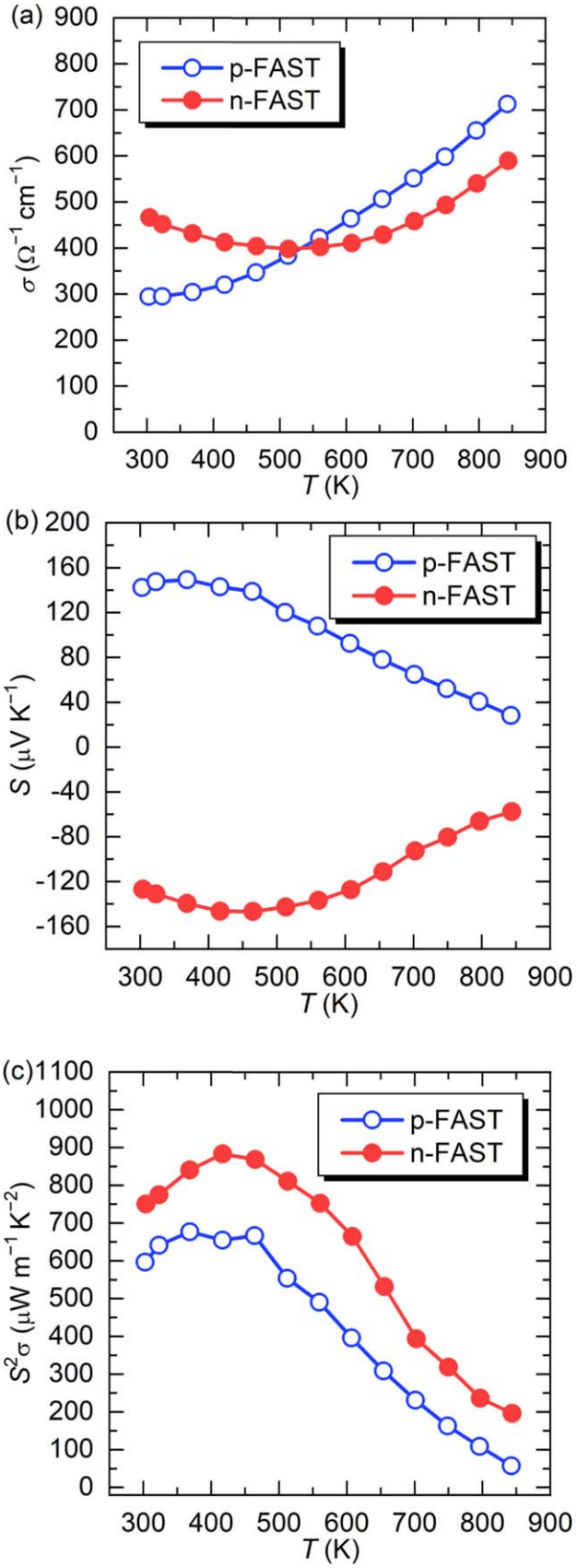

Figure 3. (a) Electrical conductivity σ, (b) Seebeck coefficient S, and (c) power factor $S^2\sigma$ of the p- and n-FAST materials plotted as a function of the temperature.

The core-level spectra of the p- and n-FAST materials for Al 2p, Al 2s, Si 2p, and Fe 3p are shown in figures 6(a)–(d), respectively. The solid curves are the raw spectra. For clarity, the spectra of the p-FAST material were shifted upward. The Al 2p core-level spectra consisted of two peaks at ~73 and ~75 eV (figure 6(a)). The

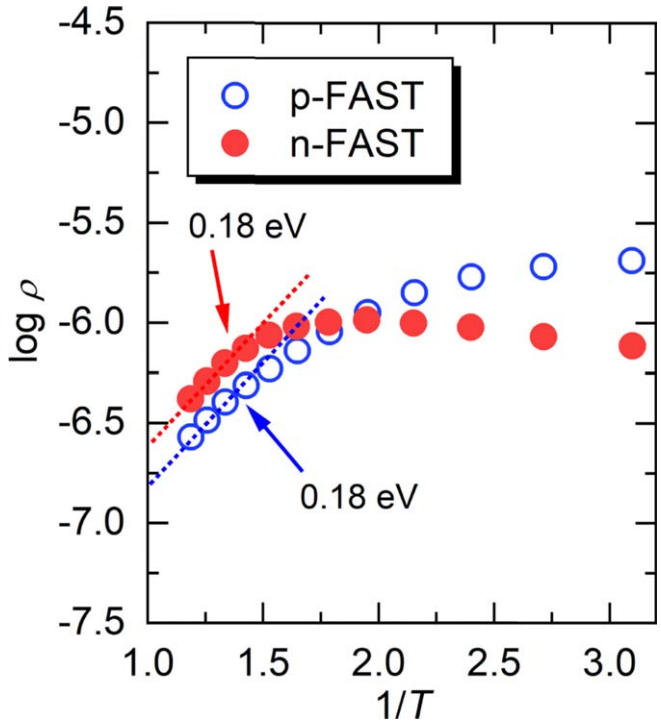

Figure 4. Natural logarithm of electrical resistivity, ρ, as a function of inverse temperature for p-and n-FAST materials.

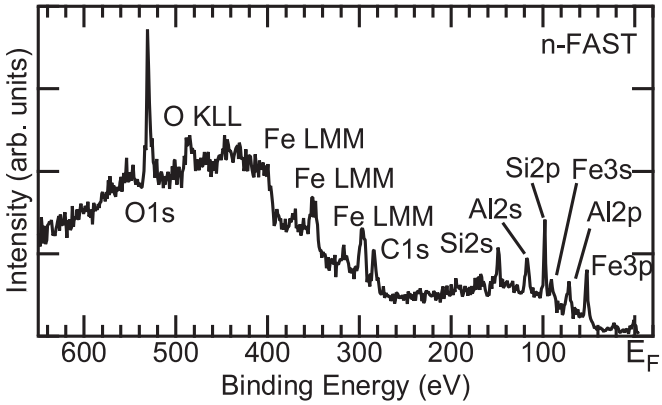

Figure 5. Typical photoemission spectrum of the n-FAST material for a wide energy range obtained by ~1000 eV excitation.

former is related to Al^0, and the latter is related to Al^{3+} [31]. We assigned the two peaks to Al^0 and Al^{3+} for simplicity, but Al^0 does not indicate ionic valency. The peak intensity of Al^{3+} showed slight position dependence, which will be discussed later. The Al 2s core-level spectra also showed two peaks at ~118 and ~120 eV (figure 6(b)). Similar to the Al 2p case, the origins of these two peaks can be assigned to the Al^0 and Al^{3+} states [31]. Similarly, the Si 2p core-level spectra showed two peaks at ~99 and ~102.5 eV (figure 6(c)). The peak at ~99 eV, which was sharper than the peak at ~102.5 eV, had a shoulder peak at higher binding energy, corresponding to $2p_{3/2}$ and $2p_{1/2}$ of Si^0 [32]. The broad hump on the higher binding-energy side probably comes from Si^{4+} [32]. In contrast to the other three elements, the core-level spectra of Fe 3p only showed a single peak with a tail toward higher binding energy (figure 6(d)). This tail may be an ionic state, such as Fe^{2+} and/or Fe^{3+} [33].

As mentioned above, the three elements showed charge-neutral states (Al^0, Si^0, and Fe^0). This compound should be metallic because the valence band is likely to be partially occupied. However, the magic electron rule, the so-called $18 - n$ rule proposed by Yannello and Fredrickson [23], can explain the electronically insulating condition for intermetallic compounds of 13- and 14-group elements (transition-metal systems). According to the magic electron rule, the number of valence states per transition metal (n_V) corresponds to $18 - n$, where 18 is the total number of states, that is, the s, p, and d orbitals with spin degrees

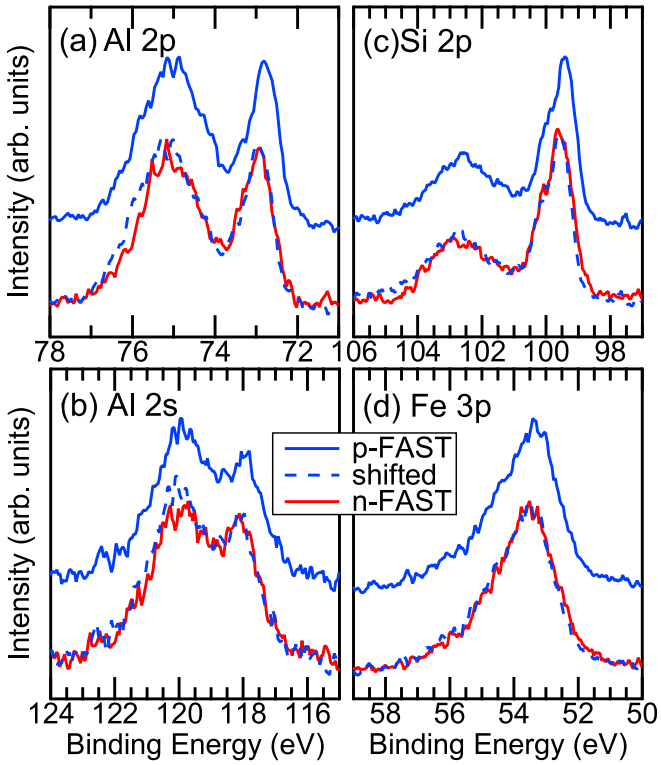

Figure 6. Photoemission spectra of the (a) Al 2p, (b) Al 2s, (c) Si 2p, and (d) Fe 3p core levels. The blue (red) curves are the spectra of p-FAST (n-FAST) material. The solid curves are the raw spectra, and the dashed curves are the spectra shifted by 0.15 eV toward higher binding energy.

of freedom of two (two states for the s orbital, six states for the p orbitals, and 10 states for the d orbitals). n is the number of covalent bonds per transition metal that form when the transition metals are located at a distance of 3 Å, corresponding to the number of antibonding states. In the case of the τ_1-$Fe_3Al_2Si_3$ compound, the number of Fe–Fe covalent bonds is four ($n = 4$). Therefore, the number of valence states per Fe atom is $n_V = 18 - 4 = 14$. In contrast, if we assume that the numbers of valence electrons of Fe, Al, and Si are 8, 3, and 4, respectively, the number of valence electrons per Fe atom (n_e) is $n_e = (8 \times 3 + 3 \times 2 + 4 \times 3)/3 = 14 = n_V$. As a result, the valence states form a closed shell and electronically insulate in the τ_1-$Fe_3Al_2Si_3$ compound. The charge-neutral states (Fe^0, Al^0, and Si^0) observed in this work support the scenario that the nearly free electrons of Al and Si occupy the Fe-based cluster orbitals. Such a cluster-based orbital description was proposed as the $5t + 4c - b$ rule by Kitahara *et al* [34] to account for electronically insulating quasicrystalline-related compounds in aluminum–transition-metal systems. This electron-counting rule is identical to the $18 - n$ rule under particular conditions.

The dashed curves in figure 6 are the spectra of the p-FAST material shifted by 0.15 eV toward the higher binding-energy side. The main peaks at lower binding energy of the n-FAST material and energy-shifted p-FAST material showed good correspondence. In contrast, the broad humps on the higher binding-energy side in the Al 2p, Al 2s, and Si 2p spectra slightly differed in their intensities. The good correspondence of the main peaks and deviation of the broad hump provide the origins of the core-level shift and broad humps, respectively. Regarding the former, the core-level shifts are mainly due to the change of the band filling in the valence band and/or conduction band through carrier doping, that is, the chemical-potential shift. In general, the core-level shift is determined by four factors: the chemical-potential shift, the change of the Madelung potential, the change of the valency, and the change of screening [35]. In the present case, all of the core-level shifts were almost identical. Because the core-level shift originated from the change of the Madelung potential, the change of the valency, and the change of screening depending on each element, site, and/or orbital, only the change of the chemical-potential can explain the observed trend. Therefore, the dominant factor of the core-level shift is the chemical-potential shift. Regarding the latter, the intensity of the broad hump showed slight spatial variation even on the same sample surface, as mentioned above. The spatial variations of the Al 2p core-level spectra for the p- and n-FAST materials are shown in figure 7. The blue and light-blue (red and orange) curves correspond to the spectra of the p-FAST (n-FAST) material. For simplicity, the peak positions of Al^0 are aligned by shifting horizontally, and the spectra of the p-FAST material are shifted vertically. Here, we normalized by the peak

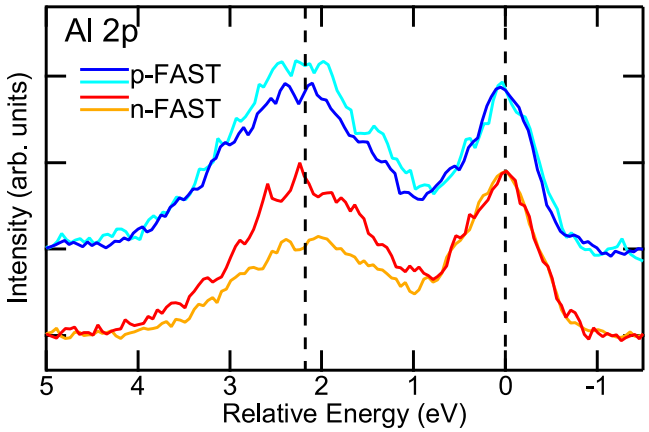

Figure 7. Photoemission spectra of Al 2p at different sample positions. The blue and light-blue (red and orange) curves are for the p-FAST (n-FAST) material. The origin of the horizontal axis is the peak position of the peak at binding energy of approximately 73 eV. The vertical dashed lines are guides for the eye for the peak positions of the main peak (~73 eV) and satellite peak (~75 eV).

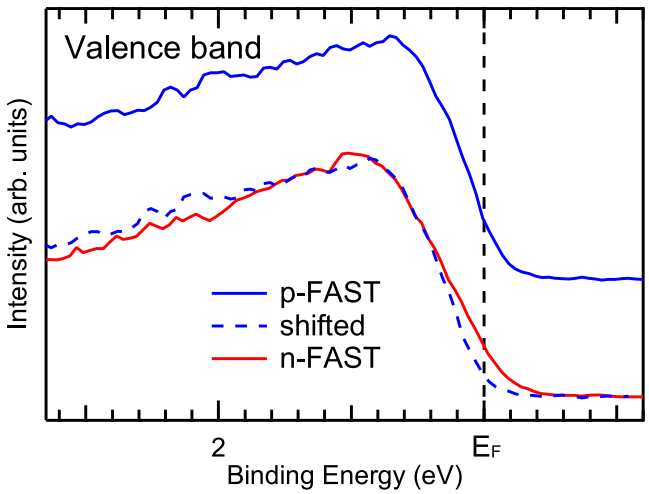

Figure 8. Valence-band spectra of the p- and n-FAST materials. The blue and red solid curves are the spectra of the p- and n-FAST materials. The dashed blue curve is the spectrum of the p-FAST material shifted by 0.15 eV toward higher binding energy.

intensities of Al^0. Because the origin of the Al^{3+} state will come from oxidized aluminum, the observed spatial variation reflects a different oxidation state.

3.3. Valence-band spectra of the doped FAST material

The photoemission spectra of the valence bands of the p- and n-FAST materials are shown in figure 8. Considering the photoemission cross section, these spectra strongly reflect Fe 3d orbitals [36]. First-principles calculations of FAST materials indicate increasing density of states toward the Fermi level down to ~1 eV and an abrupt decrease below ~1 eV [15]. This overall feature well matched the present experimental results. The dashed blue curve in figure 8 corresponds to the spectrum of the p-FAST material shifted by 0.15 eV toward higher binding energy. From figure 8, the energy positions of the highest intensities are almost the same. This indicates a rigid band shift owing to carrier doping by changing the Al/Si ratio. Because of the energy resolution of ~200 meV and the measured temperature of ~300 K, the Fermi edge is, if it exists, not clear. At least, we can safely conclude that the present samples are not good metals.

The spectral edge around the Fermi energy showed deviation. In general, photoemission spectroscopy observes occupied electronic states. In actual materials, inevitable defects and/or impurity levels may exist inside the band gap. For the n-FAST material, the Fermi level is located above the band gap or just under the bottom of the conduction band. The valence-band spectra of the n-FAST material contain much more in-gap state than that of the p-FAST material. This may be the reason for the deviation of the spectral edge.

4. Conclusions

We have synthesized high-purity polycrystalline samples of the τ_1-$Fe_3Al_2Si_3$ phase to obtain deeper insight into controlling the p-n characteristics to enhance the thermoelectric properties of FAST materials. The obtained p- and n-FAST materials showed relatively high S values of 140 and -120 μV K^{-1} at 300 K, respectively, because they had less contamination of the metallic ε-FeSi phase through optimizing the synthesis process. The photoemission spectra of the p- and n-FAST materials were consistent with the covalent bonding nature and semiconducting behavior. Because the core-level shifts were independent of the elements and orbitals, the observed chemical-potential change should be the dominant factor of the core-level shift of ∼0.15 eV, which is close to the band gap of ∼0.18 eV obtained from transport measurements.

Acknowledgments

The synchrotron radiation experiments were performed at ISSP beamline BL07LSU of SPring-8 (proposal numbers 2021A7421, 2021A7422, 2021B7433, 2021B7435, and 2022A7444). We thank Hiroyasu Kojima (Aisin Corporation) and Hitoshi Yoshimi (Aisin Takaoka Co., Ltd) for fabricating the FAST materials. We thank Edanz (https://jp.edanz.com/ac) for editing a draft of this manuscript.

Data availability statement

All data that support the findings of this study are included within the article (and any supplementary files).

Funding

This study was partially supported by JSPS KAKENHI (grant numbersphotoemission spectroscopy 20H02469, 21H01638, 21H04696, and 21K04633), JST PRESTO (JPMJPR17NB and JPMJPR20T7), and the New Energy and Industrial Technology Development Organization (NEDO).

ORCID iDs

Shunsuke Tsuda https://orcid.org/0000-0001-6209-8048
Asako Yoshinari https://orcid.org/0000-0002-8049-5028
Naoka Nagamura https://orcid.org/0000-0002-7697-8983

References

[1] Snyder G J and Toberer E S 2008 Complex thermoelectric materials *Nature Mater.* **7** 105114
[2] Freer R *et al* 2022 Key properties of inorganic thermoelectric materials—tables (version 1) *J. Phys.: Energy* **4** 022002
[3] Shi X-L, Zou J and Chen Z-G 2020 Advanced thermoelectric design: from materials and structures to devices *Chem. Rev.* **120** 7399–515
[4] Shinohara Y and Isoda Y 2007 Research and development of iron disilicide thermoelectric material from the viewpoint of function units constituting lattice *J. Jpn. Ins. Met.* **71** 869–75
[5] Miyazaki Y, Igarashi D, Hayashi K, Kajitani T and Yubuta K 2008 Modulated crystal structure of chimney-ladder higher manganese silicides $MnSi_\gamma$ ($\gamma \sim 1.74$) *Phys. Rev.* B **78** 214104
[6] Nishino Y, Kato M, Asano S, Soda K, Hayashi M and Mizutani U 1997 Semiconductorlike behavior of electrical resistivity in heusler-type Fe_2VAl compound *Phys. Rev. Lett.* **79** 1909–12
[7] Ying P, He R, Mao J, Zhang Q, Reith H, Sui J, Ren Z, Nielsch K and Schierning G 2021 Towards tellurium-free thermoelectric modules for power generation from low-grade heat *Nat. Commun.* **12** 1121
[8] Mulla R and Rabinal M H K 2017 Copper sulfides: earth-abundant and low-cost thermoelectric materials *Energy Technol.* **7** 1800850
[9] Sun Y, Christensen M, Johnsen S, Nong N V, Ma Y, Sillassen M, Zhang E, Palmqvist A E C, Bøttiger J and Iversen B B 2012 Low-cost high-performance zinc antimonide thin films for thermoelectric applications *Adv. Mater.* **24** 1693–6
[10] Takagiwa Y, Isoda Y, Goto M and Shinohara Y 2018 Electronic structure and thermoelectric properties of narrow-band-gap intermetallic compound $Al_2Fe_3Si_3$ *J. Therm. Anal. Calorim.* **131** 281–7
[11] Shiota Y, Muta H, Yamamoto K, Ohishi Y, Kurosaki K and Yamanaka S 2017 A new semiconductor $Al_2Fe_3Si_3$ with complex crystal structure *Intermetallics* **89** 51–6
[12] Takagiwa Y, Ikeda T and Kojima H 2020 Earth-abundant Fe–Al–Si thermoelectric (FAST) materials: from fundamental materials research to module development *ACS Appl. Mater. Interfaces* **12** 48804–10
[13] Takagiwa Y, Hou Z, Tsuda K, Ikeda T and Kojima H 2021 Fe–Al–Si thermoelectric (FAST) materials and modules: diffusion couple and machine-learning-assisted materials development *ACS Appl. Mater. Interfaces* **13** 53346–54
[14] Takagiwa Y and Shinohara Y 2019 A practical appraisal of thermoelectric materials for use in an autonomous power supply *Scripta Mater.* **172** 98–104
[15] Hou Z, Takagiwa Y, Shinohara Y, Xu Y and Tsuda K 2021 First-principles study of electronic structures and elasticity of $Al_2Fe_3Si_3$ *J. Phys. Condens. Matter* **33** 195501

[16] Takagiwa Y, Isoda Y, Goto M and Shinohara Y 2018 Conduction type control and power factor enhancement of the thermoelectric material $Al_2Fe_3Si_3$ *J. Phys. Chem. Solids* **118** 95–8
[17] Shiota Y, Yamamoto K, Ohishi Y, Kurosaki K and Muta H 2018 Thermoelectric properties of Co- and Mn-doped $Al_2Fe_3Si_3$ *J. Electron. Mater.* **48** 475–82
[18] Srinithi A K, Sepehri-Amin H, Takagiwa Y and Hono K 2022 Effect of microstructure on the electrical conductivity of p-type Fe–Al–Si thermoelectric materials *J. Alloys. Compds.* **903** 163835
[19] Schlesinger Z, Fisk Z, Zhang H-T, Maple M B, DiTusa J F and Aeppli G 1993 Unconventional charge gap formation in FeSi *Phys. Rev. Lett.* **71** 1748–51
[20] Weinert M and Watson R E 1998 Hybridization-induced band gaps in transition-metal aluminides *Phys. Rev.* B **58** 9732–40
[21] Fredrickson D C, Lee S, Hoffmann R and Lin J 2004 The nowotny chimney ladder phases: following the c_{pseudo} clue toward an explanation of the 14 electron rule *Inorg. Chem.* **43** 6151–8
[22] Fredrickson D C, Lee S and Hoffmann R 2004 The nowotny chimney ladder phases: whence the 14 electron rule? *Inorg. Chem.* **43** 6159–67
[23] Yannello V J and Fredrickson D C 2015 Generality of the 18-n rule: intermetallic structural chemistry explained through isolobal analogies to transition metal complexes *Inorg. Chem.* **54** 11385–98
[24] Zeier W G, Zevalkink A, Gibbs Z M, Hautier G, Kanatzidis M G and Snyder G J 2016 Thinking like a chemist: intuition in thermoelectric materials *Angew. Chem.* **55** 6826–41
[25] Soda K *et al* 2002 High-resolution photoelectron spectroscopy of heusler-type Fe_2VAl alloy *J. Synchrotron Rad.* **9** 233–6
[26] Heremans J P, Wiendlocha B and Chamoire A M 2012 Resonant levels in bulk thermoelectric semiconductors *Energy Environ. Sci.* **5** 5510–30
[27] Raghavan V 2009 Al-Fe-Si (Aluminum-iron-silicon) *J. Phase Equilibria Diffus.* **30** 184–8
[28] Marker M C J, Skolyszewska-Kühberger B, Effenberger H S, Schmetterer C and Richter K W 2011 Phase equilibria and structural investigations in the system Al–Fe–Si *Intermetallics* **19** 1919–29
[29] Horiba K, Nakamura Y, Nagamura N, Toyoda S, Kumigashira H, Oshima M, Amemiya K, Senba Y and Ohashi H 2011 Scanning photoelectron microscope for nanoscale three-dimensional spatial-resolved electron spectroscopy for chemical analysis *Rev. Sci. Instrum.* **82** 113701
[30] Shirley D A 1972 High-resolution x-ray photoemission spectrum of the valence bands of gold *Phys. Rev.* B **5** 4709
[31] Sherwood P M A 1998 Introduction to studies of aluminum and its compounds by XPS *Surf. Sci. Spectra* **5** 1
[32] Oh J H, Yeom H W, Hagimoto Y, Ono K, Oshima M, Hirashita N, Nywa M, Toriumu A and Kakizaki A 2001 Chemical structure of the ultrathin SiO_2/Si(100) interface: An angle-resolved Si 2p photoemission study *Phys. Rev.* B **63** 205310
[33] Yang D-Q and Sacher E 2009 Characterization and oxidation of fe nanoparticles deposited onto highly oriented pyrolytic graphite, using x-ray photoelectron spectroscopy *J. Phys. Chem.* C **113** 6418–25
[34] Kitahara K, Takagiwa Y and Kimura K 2017 Unified cluster-based description of valence bands in AlIr, $RuAl_2$ $RuGa_3$ and Al–TM quasicrystalline approximants *J. Phys. Conf. Ser.* **809** 012014
[35] Hüfner S 2003 *Photoelectron Spectroscopy* (Berlin: Springer)
[36] Yeh J J and Lindau I 1985 Atomic subshell photoionization cross sections and asymmetry parameters: $1 \leqslant Z \leqslant 103$ *At. Data Nucl. Data Tables* **32** 1